INTERNATIONAL JOURNAL FOR NUMERICAL METHODS IN FLUIDS
Int. J. Numer. Meth. Fluids 2000; **34**: 113–144

Analysis of flow in the plate-spiral of a reaction turbine using a streamline upwind Petrov–Galerkin method

P. K. Maji and G. Biswas*,[1]

Department of Mechanical Engineering, Indian Institute of Technology, Kanpur, India

SUMMARY

The prediction of the flow field in a novel spiral casing has been accomplished. Hydraulic turbine manufacturers are considering the potential of using a special type of spiral casing because of the easier manufacturing process involved in its fabrication. These special spiral casings are known as plate-spirals. Numerical simulation of complex three-dimensional flow through such spiral casings has been accomplished using a finite element method (FEM). An explicit Eulerian velocity correction scheme has been deployed to solve the Reynolds-average Navier–Stokes equations. The simulation has been performed to describe the flow in high Reynolds number (10^6) regimes. For spatial discretization, a streamline upwind Petrov–Galerkin (SUPG) technique has been used. The velocity field and the pressure distribution inside the spiral casing reveal meaningful results. Copyright © 2000 John Wiley & Sons, Ltd.

KEY WORDS: finite element method; hydraulic turbine; plate-spiral; spiral casing; streamline upwind Petrov–Galerkin technique; weak formulation

1. INTRODUCTION

The spiral casing of a hydraulic turbine is a passage with a 360° turn to direct water, entering one end, to exit circumferentially along the radial inward direction. The role of the spiral casing in a Francis or Kaplan turbine is to distribute the water, as evenly as possible, to the stay vanes and wicket gates and then to the turbine runner. In a good spiral casing, the pressure head of fluid is made available to the runner with minimum loss, hence the analysis of the flow through a spiral casing is important for the efficient design of hydraulic turbines. Very few articles are available in the literature on the computational analysis of this problem.

The assumption that the spiral casing can be modeled by using potential flow with acceptable accuracy has been proven by Sopta *et al.* [1] and Mrsa [2]. Ulrich [3] has modeled the viscous flow in a spiral casing and described the flow structure for the first time. He used Galerkin's finite element based technique for his analysis. However, his studies were restricted

* Correspondence to: Department of Mechanical Engineering, Indian Institute of Technology, Kanpur 208 016, India.
[1] E-mail: gtm@iitk.ac.in

Received March 1999
Revised August 1999

for low Reynolds number regimes. Thereafter, Shyy and Vu [4,9,10], Vu *et al.* [5], Vu and Shyy [6–8] have conducted several important investigations for predicting the flow characteristics and energy losses in different parts of the hydraulic turbine.

Figure 1 shows the spiral casing, the stay vanes, the runner, and the draft tube of a hydraulic turbine. In a modified configuration, the entire set of the stay vanes and the guide vanes can be housed in the gap between two circular disks attached to the spiral casing. Such an arrangement is usually referred as the *plate-spiral*. The sectional view of the plate-spiral is shown in Figure 2. The outer diameter of the disk is called the exterior diameter. The terminology WGID, WGOD, SVID, and SVOD mean *wicket gate inner diameter*, *wicket gate outer diameter*, *stay vane inner diameter*, and *stay vane outer diameter* respectively. The hydraulic turbine manufacturers are considering the potential use of such spirals. However, the detailed performances of such spirals are not known. Model testing of new spirals is also quite expensive. A need has been felt to develop a computational tool for analyzing spirals of various shapes and sizes.

The aim of this work is to predict the flow structure and pressure drop characteristics in a plate-spiral, which can be used for Francis and/or Kaplan turbines. For the modeling of high Reynolds number flow in the spiral casing, a simplified turbulence model has been used.

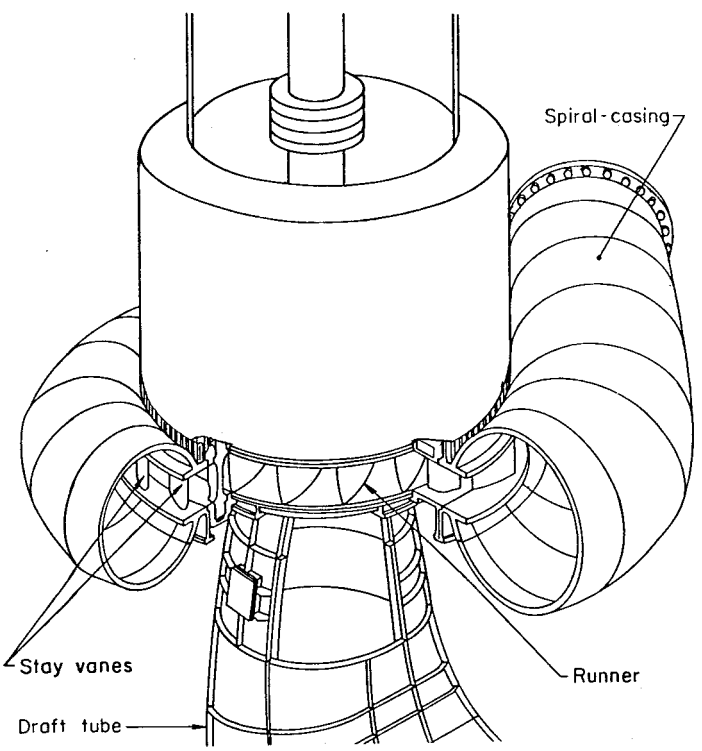

Figure 1. Spiral casing of a hydraulic turbine.

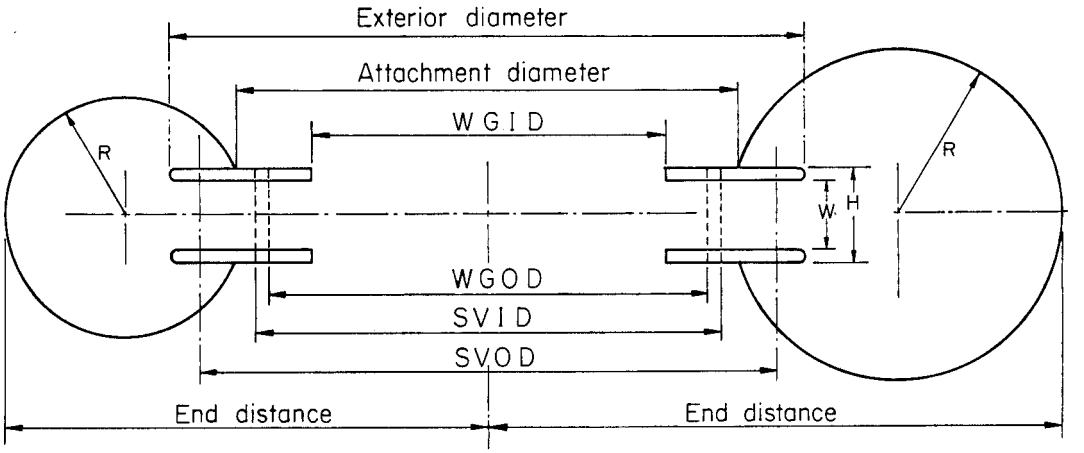

Figure 2. Cross-sectional view of the plate-spiral.

For generating the finite element mesh in the above-mentioned geometry, initially two-dimensional grids are generated at 34 cross-sectional planes along the flow direction. Thereafter, three-dimensional grids have been formed by connecting the consecutive cross-planes at the corresponding nodes. A transfinite interpolation technique (Sundararajan [11]) has been used for the generation of the mesh. Figure 3 shows the three-dimensional view of the grid mesh.

The *streamline upwind Petrov–Galerkin* (SUPG) technique (Brooks and Hughes [12]) has been deployed to solve the three-dimensional Reynolds-averaged Navier–Stokes equations in the above-mentioned geometry.

2. GOVERNING EQUATIONS AND THE SOLUTION SCHEME

The flow is considered to be viscous, incompressible, and turbulent. The geometry of interest is three-dimensional. The computational domain is discretized into small hexahedral elements. The velocity components and the pressure are collocated at each node of the element. The Reynolds averaged Navier–Stokes equations for incompressible flows, with an extra term indicating the porous medium treatment based on Darcy's law, have been used here as governing equations. These equations, together with the mass conservation equations, can be written in the Cartesian tensor form as

$$\frac{\partial u_i}{\partial x_i} = 0 \tag{1}$$

$$\frac{\mathrm{D}u_j}{\mathrm{D}\tau} = -\frac{\partial p}{\partial x_j} + \frac{1}{Re}\frac{\partial}{\partial x_i}\left[(1+\nu_{t,n})\left(\frac{\partial u_i}{\partial x_j}+\frac{\partial u_j}{\partial x_i}\right)\right] - Ku_j \tag{2}$$

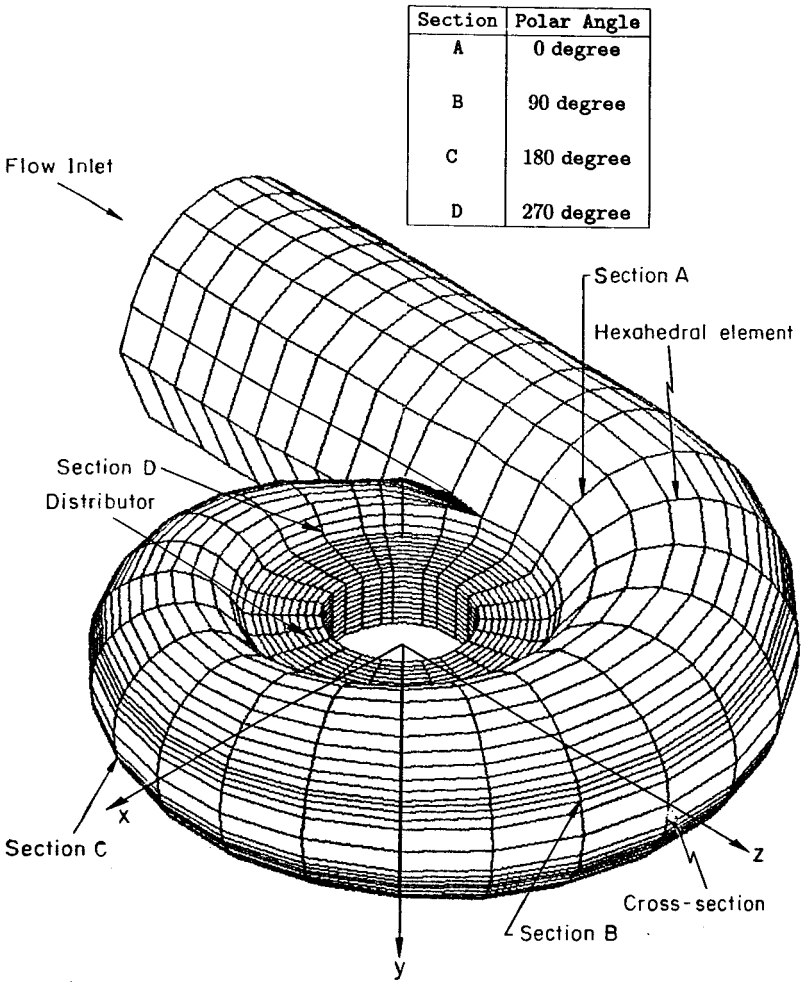

Figure 3. Grid for the spiral casing.

The subscripts i and j can take the values 1, 2, or 3 in three co-ordinate directions, x_1, x_2, and x_3 respectively. The x_1, x_2, and x_3 are equivalent to x, y, and z in Cartesian co-ordinates and the velocity u_1, u_2, and u_3 are equivalent to u, v, and w respectively. The equations have been written in the dimensionless form, which facilitates the generalization to embody a large range of problems. Here

$$Re = \frac{W_0 D}{v}$$

where D is the characteristic length, v is the kinematic viscosity, and W_0 is the inlet velocity. The non-dimensional turbulent viscosity $v_{t,n}$ is given by Prandtl's mixing length model as

$$v_{t,n} = l_n^2 Re\left[\left(\frac{\partial u_i}{\partial x_j} + \frac{\partial u_j}{\partial x_i}\right)\frac{\partial u_i}{\partial x_j}\right]^{1/2} \tag{3}$$

This is known as the zero-equation model. The zero-equation models obviously have several shortcomings, which are indicated in the turbulent flow literature. Since the geometry itself is extremely complex, at this stage the turbulent flow has been dealt with a simple model. Albeit this simplification, all the subtle features of engineering importance are highlighted through this simulation. In any case, in Equation (3), l_n is given by $\lambda\delta$, where δ is the non-dimensional radius of the duct at any section and λ is a constant (chosen as 0.085).

The term K is the Darcy's coefficient, whose value indicates the resistance due to the porous medium in the distributor region (Figure 3). As such, the distributor has 18 pairs of aerofoils that control the mass flux distribution of fluid. The fluid enters the runner after leaving the distributor zone. Since the spiral casing and the distributor influence each other significantly, both are to be treated simultaneously. In order to predict the flow behavior inside the spiral casing, the distributor zone has been considered as a porous medium and the effect of the individual aerofoil has been smeared out.

2.1. Eulerian velocity correction approach

This method is essentially based on the projection scheme of Chorin [13], which was originally developed in a finite difference context and identical to the marker and cell (MAC) method of Harlow and Welch [14]. This has been extended to the finite element method (FEM) by Donea *et al.* [15]. In the present study, the algorithm has been extended to the solution of turbulent flow in a complex geometry. The complete algorithm has been presented by Maji and Biswas [16] elsewhere. However, some salient features of the algorithm are being presented herein for a ready reference.

The Eulerian velocity correction method is a solution algorithm for unsteady, incompressible Navier–Stokes equations. The solution at each time step is obtained through three steps.

STEP 1: Calculation of Provisional Velocities

The provisional velocities are calculated from the momentum equations by dropping the pressure terms

$$\frac{\partial u_j^*}{\partial \tau} = -\left(u_i \frac{\partial u_j}{\partial x_i}\right) + \frac{1}{Re}\frac{\partial}{\partial x_i}\left[(1 + v_{t,n})\left(\frac{\partial u_i}{\partial x_j} + \frac{\partial u_j}{\partial x_i}\right)\right] - Ku_j \tag{4}$$

The above form of equations is used to calculate the provisional velocities u^*, v^*, and w^*.

STEP 2: Solution of Pressure Equation

The pressure term, which was initially ignored, may be taken into account now. Thus, the momentum equations become

$$\frac{\partial u_j}{\partial \tau} = -\frac{\partial p}{\partial x_j} + \frac{\partial u_j^*}{\partial \tau} \tag{5}$$

Expanding the above equation in the time domain, the following equation is obtained:

$$u_j^{n+1} = u_j^* - \Delta\tau \left(\frac{\partial p}{\partial x_j}\right)^{n+1} \tag{6}$$

Differentiating Equation (6) with respect to x, y, and z for $j = 1$, 2, and 3 respectively, then adding the three and rearranging, one obtains

$$[\nabla^2 p]^{n+1} = \frac{1}{\Delta\tau}\left(\frac{\partial u_i^*}{\partial x_i}\right) \tag{7}$$

In the above derivation, $(\partial u_i/\partial x_i)^{n+1}$ has been equated to zero.

STEP 3: Velocity Correction

The velocities are corrected at the next time step by updating the provisional velocities using the evaluated pressure. Equation (6) is used to calculate the velocities u^{n+1}, v^{n+1}, and w^{n+1}.

Here one can interpret the role of pressure in the momentum equations as a projection operator that projects an arbitrary vector field into a divergence free vector field.

The salient features of the above-mentioned solution procedure may be summarized as

1. Start with initial conditions of $(u_j)_0$; p_0; $n = 0$.
2. Calculate the provisional velocities u_j^* from Equation (4) using the explicit Euler's scheme.
3. Calculate the pressure p^{n+1} using Equation (7).
4. Calculate the corrected velocities u_j^{n+1} from Equation (6).

The above-mentioned steps are repeated till a steady state condition is reached.

2.2. Galerkin weighted residual method

Let Ω (geometry of interest) be a bounded region in $\Re^3$ with the piecewise smooth boundary Γ. Let $\mathbf{x} = \{x_i\}$, $i = 1, 2, 3$, denote the vector of spatial co-ordinates of a general point in $\bar{\Omega}$ and let τ denote the time value in the interval $J = [0, T]$. Also consider $\vec{n}$ as the outward normal vector to Γ, and Γ_g and Γ_h as non-overlapping regions of Γ that satisfy the following:

$$\overline{\Gamma_g \cup \Gamma_h} = \Gamma \tag{8}$$

$$\Gamma_g \cap \Gamma_h = \varnothing \tag{9}$$

The superimposed bar in Equation (8) represents set closure and $\varnothing$ in Equation (9) denotes the empty set. Now, our focus is on the finite element formulation of the problem defined by Equations (4), (5), and (7), along with the following boundary conditions:

- Boundary and initial conditions for velocities

$$u_j(\{x_i\}, \tau) = g_j, \quad \forall\{x_i\} \in \Gamma_g, \quad \forall\tau \in [0, t_n], \quad t_n > 0;$$

$$\vec{n} \cdot \nabla u_j = h_j, \quad \forall\{x_i\} \in \Gamma_h, \quad \forall\tau \in [0, t_n], \quad t_n > 0;$$

$$u_j(\{x_i\}, 0) = (u_j)_0 \tag{10}$$

- Boundary and initial conditions for pressure

$$p(\{x_i\}, \tau) = s, \quad \forall\{x_i\} \in \Gamma_h, \quad \forall\tau \in [0, t_n], \quad t_n > 0;$$

$$\vec{n} \cdot \nabla p = b, \quad \forall\{x_i\} \in \Gamma_g, \quad \forall\tau \in [0, t_n], \quad t_n > 0;$$

$$p(\{x_i\}, 0) = p_0 \tag{11}$$

where g_j, h_j, s, b are given functions of x, y, z, and τ. The initial condition $(u_j)_0$ and p_0 are the given functions of x, y, and z. The first step of an FEM is to write the weak formulation of Equations (4), (5), and (7).

2.3. Weak formulation

Let S and V be the vector spaces of the admissible trial (basis/shape) and test (weighting) functions, which may be defined as

$$S = \{\Phi(\Omega) \big| \Phi \in (H^1(\Omega))^4, \ \Phi = \Phi_g \ \text{ on } \ \Gamma_g^*\} \tag{12}$$

where $\Gamma_g^* = \Gamma_g$ when velocities are specified; $\Gamma_g^* = \Gamma_g$ when pressure is specified; $\Phi = \{u_j, p\}$; $\Phi_g = \{g_j, s\}$; and

$$V = \{W \big| W \in H^1(\Omega), \ W = 0 \ \text{ on } \ \Gamma_g^*\} \tag{13}$$

where $H^1(\Omega)$ is the space of the functions that, together with their first partial derivatives, are square integrable in Ω.

Multiplying Equation (4) by W, and integrating over Ω yields

$$\int_\Omega W\left[\frac{\mathrm{D}u_j^*}{\mathrm{D}\tau} - \frac{1}{Re}\left\{\frac{\partial}{\partial x_i}\left[(1 + \nu_{\mathrm{t},n})\left(\frac{\partial u_i}{\partial x_j} + \frac{\partial u_j}{\partial x_i}\right)\right]\right\} + Ku_j\right] \mathrm{d}\Omega = 0 \tag{14}$$

where

$$\frac{\mathrm{D}u_j^*}{\mathrm{D}\tau} = \frac{\partial u_j^*}{\partial \tau} + u_i \frac{\partial u_j}{\partial x_i}$$

Application of Green's theorem to the diffusion term of above equation and invoking $W = 0$ on Γ_g and $(\partial u_j/\partial x_i)n_i = \partial u_j/\partial n = h_j$ (see Equation (10)), the above equation reduces to

$$\int_\Omega W\left[\frac{\mathrm{D}u_j^*}{\mathrm{D}\tau} + Ku_j\right]\mathrm{d}\Omega + \frac{1}{Re}\int_\Omega \left[\frac{\partial W}{\partial x_i}(1+v_{\mathrm{t},n})\left(\frac{\partial u_i}{\partial x_j}+\frac{\partial u_j}{\partial x_i}\right)\right]\mathrm{d}\Omega$$
$$-\frac{1}{Re}\int_{\Gamma_h} W(1+v_{\mathrm{t},n})\left(\frac{\partial u_i}{\partial x_j}n_i + h_j\right)\mathrm{d}\Gamma = 0 \tag{15}$$

Now multiplying Equation (5) by W and integrating over Ω yields

$$\int_\Omega W\left[\frac{\partial u_j}{\partial \tau} - \frac{\partial u_j^*}{\partial \tau} + \frac{\partial p}{\partial x_j}\right]\mathrm{d}\Omega = 0 \tag{16}$$

Similarly, Equation (7) reduces to

$$\int_\Omega \frac{\partial W}{\partial x_i}\frac{\partial p}{\partial x_i}\,\mathrm{d}\Omega = \int_{\Gamma_g} W\frac{\partial p}{\partial n}\,\mathrm{d}\Gamma - \frac{1}{\Delta\tau}\int_\Omega W\frac{\partial u_i^*}{\partial x_i}\,\mathrm{d}\Omega \tag{17}$$

2.4. Finite element formulation

In order to find a discrete solution of Equations (15)–(17), we assume Ω is discretized in N_e hexahedral elements such that

$$\bigcup_{e=1}^{N_e}\overline{\Omega^e} = \bar{\Omega}, \qquad \bigcap_{e=1}^{N_e}\Omega^e = \varnothing \tag{18}$$

where Ω^e denotes the interior domain of an element. Let Γ^e be the boundary of Ω^e. Finally, the 'interior boundary' Γ_{int} is defined as the following:

$$\Gamma_{\mathrm{int}} = \bigcup_{e=1}^{N_e}\Gamma^e - \Gamma \tag{19}$$

Let (u_i^h, p^h) be a member of S^h and W^h be member of V^h, where S^h and V^h are finite dimensional sub-spaces of the trial (S) and test (V) spaces respectively, and defined as

$$S^h = \{(u_i^h, p^h) \in (C^0(\Omega))^4,\ u_i^h = g_i,\ \text{and}\ p^h = s\ \text{ on }\ \Gamma_g^*\}$$

$$V^h = \{W^h \in C^0(\Omega),\ W^h = 0\ \text{ on }\ \Gamma_g^*\}$$

Now, FEMs can be formulated by requiring the discrete solution u_i^h, p^h to satisfy the weak form of Equations (15)–(17).

Thus, Equation (15) becomes

$$\int_\Omega W^h\left(\frac{\mathrm{D}(u_j^h)^*}{\mathrm{D}\tau}+Ku_j^h\right)\mathrm{d}\Omega+\frac{1}{Re}\int_\Omega\frac{\partial W^h}{\partial x_i}(1+v_{\mathrm{t},n}^h)\left(\frac{\partial u_i^h}{\partial x_j}+\frac{\partial u_j^h}{\partial x_i}\right)\mathrm{d}\Omega$$
$$-\frac{1}{Re}\int_{\Gamma_h}W^h(1+v_{\mathrm{t},n}^h)\left(\frac{\partial u_i^h}{\partial x_j}n_i+h_j\right)\mathrm{d}\Gamma=0 \tag{20}$$

In a similar manner, Equation (16) becomes

$$\int_\Omega W^h\frac{\partial u_j^h}{\partial\tau}\,\mathrm{d}\Omega=\int_\Omega W^h\frac{\partial(u_j^h)^*}{\partial\tau}\,\mathrm{d}\Omega-\int_\Omega W^h\frac{\partial p^h}{\partial x_j}\,\mathrm{d}\Omega \tag{21}$$

Following a similar approach, Equation (17) becomes

$$\int_\Omega\frac{\partial W^h}{\partial x_i}\frac{\partial p^h}{\partial x_i}\,\mathrm{d}\Omega=\int_{\Gamma_g}W^hb\,\mathrm{d}\Gamma-\frac{1}{\Delta\tau}\int_\Omega W^h\frac{\partial(u_i^h)^*}{\partial x_i}\,\mathrm{d}\Omega \tag{22}$$

Let the finite set $\{N_i\}$ represent a basis for S^h, while $\{W_i\}$ is the basis for V^h. The functions N_i and W_i are associated with the node i of the finite element mesh. The discrete solution u_i^h, p^h can be approximated within each element as a linear combination of the trial (basis) functions as follows:

$$u_i^h=\sum_{m=1}^{N_p}(u_i(\tau))_mN_m=\{N\}^T\{u_i(\tau)\}$$

$$p^h=\sum_{m=1}^{N_p}(p(\tau))_mN_m=\{N\}^T\{p(\tau)\} \tag{23}$$

where N_p is the total number of nodes in each element and $\{N\}$ represents a column matrix of dimension $1\times N_p$ and $\{N\}^T$ represents the transpose of $\{N\}$. The trial functions $\{N\}$ are piecewise trilinear and can be expressed in terms of the transformed local co-ordinates (ξ,η,ζ). With the approximation of u_i^h and p^h invoking the concept of mass lumping and mapping eight-noded hexahedral elements onto a $2\times2\times2$ cube via isoparametric transformation, Equations (21) and (22) become

- *Velocity correction equations*

$$\sum_{e=1}^{N_e}\int_{\Omega^e}[N]\,\mathrm{d}\Omega\{u_j^{n+1}\}=\sum_{e=1}^{N_e}\int_{\Omega^e}[N]\,\mathrm{d}\Omega\{u_j^*\}-\Delta\tau\sum_{e=1}^{N_e}\int_{\Omega^e}[N]\,\mathrm{d}\Omega\left\{\frac{\partial p^{n+1}}{\partial x_j}\right\} \tag{24}$$

- *Pressure Poisson equation*

$$\sum_{e=1}^{N_e} \int_{\Omega^e} \left\{\frac{\partial N}{\partial x_i}\right\}\left\{\frac{\partial N}{\partial x_i}\right\}^T \mathrm{d}\Omega\{p^{n+1}\} = -\frac{1}{\Delta\tau}\sum_{e=1}^{N_e} \int_{\Omega^e} \{N\}\left\{\frac{\partial N}{\partial x_i}\right\}^T \{u_i^*\}\,\mathrm{d}\Omega + \sum_l \int_{\Gamma_g^l} \{N\}b\,\mathrm{d}\Gamma \tag{25}$$

2.5. Streamline upwind Petrov–Galerkin based technique

The numerical scheme based on the standard Galerkin (Bubnov–Galerkin) FEM for convection–diffusion problems experiences poor convergence when convection dominates over diffusion. Several upwind-biased finite element formulations have been proposed by many researchers to deal with such situations. Many of the proposed schemes, when applied to a multi-dimensional problem suffer from cross-wind diffusion, which is similar to those encountered in finite difference and finite volume based approaches. To overcome this cross-wind problem, Brooks and Hughes [12] introduced the SUPG technique with the application of modified weighting functions for all terms of the governing equations. The SUPG formulation uses the trial functions and the test functions from different classes of functional space. In a usual Galerkin weighted residual method, the test (weighting) functions are to be continuous across inter-element boundaries. However, the SUPG formulation requires discontinuous test functions of the form

$$\bar{W}^h = W^h + U^h \tag{26}$$

where W^h is a continuous weighting function and U^h is the discontinuous streamline upwind contribution. Both W^h and U^h are assumed to be smooth on the element interiors.

The SUPG based finite element formulation for Equation (20) is written as

$$\begin{aligned}
&\sum_{e=1}^{N_e} \int_{\Omega^e} W^h\left(\frac{\partial (u_j^h)^*}{\partial\tau} + u_i^h\frac{\partial u_j^h}{\partial x_i} + Ku_j^h\right)\mathrm{d}\Omega + \frac{1}{Re}\sum_{e=1}^{N_e}\int_{\Omega^e}\frac{\partial W^h}{\partial x_i}(1+v_{\mathrm{t},n}^h)\left(\frac{\partial u_i^h}{\partial x_j}+\frac{\partial u_j^h}{\partial x_i}\right)\mathrm{d}\Omega\\
&-\frac{1}{Re}\int_{\Gamma_h} W^h(1+v_{\mathrm{t},n}^h)\left(\frac{\partial u_i^h}{\partial x_j}n_i + h_j\right)\mathrm{d}\Gamma\\
&+\sum_{e=1}^{N_e}\int_{\Omega^e} U^h\left\{\frac{\partial (u_j^h)^*}{\partial\tau} + u_i^h\frac{\partial u_j^h}{\partial x_i} - \frac{1}{Re}\frac{\partial}{\partial x_i}\left((1+v_{\mathrm{t},n}^h)\left(\frac{\partial u_i^h}{\partial x_j}+\frac{\partial u_j^h}{\partial x_i}\right)\right) + Ku_j^h\right\}\mathrm{d}\Omega = 0
\end{aligned} \tag{27}$$

Applying Green's theorem to the second term of above equation and invoking $\bar{W}^h$ in the above expression, the following equation may be obtained:

$$\begin{aligned}
&\sum_{e=1}^{N_e}\int_{\Omega^e}\bar{W}^h\left[\frac{\partial (u_j^h)^*}{\partial\tau} + u_i^h\frac{\partial u_j^h}{\partial x_i} - \frac{1}{Re}\left\{\frac{\partial}{\partial x_i}\left[(1+v_{\mathrm{t},n}^h)\left(\frac{\partial u_i^h}{\partial x_j}+\frac{\partial u_j^h}{\partial x_i}\right)\right]\right\} + Ku_j^h\right]\mathrm{d}\Omega\\
&+\frac{1}{Re}\int_{\cup_{e=1}^{N_e}\Gamma^e} W^h(1+v_{\mathrm{t},n}^h)\left(\frac{\partial u_i^h}{\partial x_j}+\frac{\partial u_j^h}{\partial x_i}\right)n_i\,\mathrm{d}\Gamma - \frac{1}{Re}\int_{\Gamma_h} W^h(1+v_{\mathrm{t},n}^h)\left(\frac{\partial u_i^h}{\partial x_j}n_i + h_j\right)\mathrm{d}\Gamma = 0
\end{aligned} \tag{28}$$

Let the diffusive flux in the normal direction and boundary be

$$(\sigma_j^d)_n = \frac{1+\nu_{t,n}^h}{Re}\left(\frac{\partial u_i^h}{\partial x_j}+\frac{\partial u_j^h}{\partial x_i}\right)n_i = (\sigma_j^d)_i n_i \tag{29}$$

and

$$H_j = \frac{1+\nu_{t,n}^h}{Re}\left(\frac{\partial u_i^h}{\partial x_j}n_i + h_j\right) \tag{30}$$

We also know from Equation (19) that

$$\bigcup_{e=1}^{N_e}\Gamma^e = \Gamma_{\text{int}} + \Gamma = \Gamma_{\text{int}} + \Gamma_g + \Gamma_h$$

With these definitions and also considering $W^h = 0$ on Γ_g, Equation (28) can be written as

$$\sum_{e=1}^{N_e}\int_{\Omega^e}\bar{W}^h\left[\frac{\partial (u_j^h)^*}{\partial\tau}+u_i^h\frac{\partial u_j^h}{\partial x_i}-\frac{1}{Re}\left\{\frac{\partial}{\partial x_i}\left[(1+\nu_{t,n}^h)\left(\frac{\partial u_i^h}{\partial x_j}+\frac{\partial u_j^h}{\partial x_i}\right)\right]\right\}+Ku_j^h\right]d\Omega$$
$$+\int_{\Gamma_{\text{int}}}W^h[(\sigma_j^d)_n]\,d\Gamma+\int_{\Gamma_h}W^h\{(\sigma_j^d)_n-H_j\}\,d\Gamma=0 \tag{31}$$

where $[\,(\sigma_j^d)_n\,]$ represent the jump in $(\sigma_j^d)_n$ across inter-element boundaries.

The diffusion continuity condition across inter-element boundaries satisfies the following:

$$[(\sigma_j^d)_n]=0 \quad \text{across } \Gamma_{\text{int}}$$

Also on Γ_h

$$(\sigma_j^d)_n = H_j \tag{32}$$

Substitution of Equation (32) into Equation (31) yields

$$\sum_{e=1}^{N_e}\int_{\Omega^e}\bar{W}^h\left(\frac{\partial (u_j^h)^*}{\partial\tau}\right)d\Omega$$
$$=-\sum_{e=1}^{N_e}\int_{\Omega^e}\bar{W}^h\left(u_i^h\frac{\partial u_j^h}{\partial x_i}\right)d\Omega-\sum_{e=1}^{N_e}\int_{\Omega^e}\bar{W}^h(Ku_j^h)\,d\Omega+\int_{\Gamma_h}W^hH_j\,d\Gamma$$
$$-\sum_{e=1}^{N_e}\int_{\Omega^e}\frac{\partial W^h}{\partial x_i}\left\{\frac{(1+\nu_{t,n}^h)}{Re}\left(\frac{\partial u_i^h}{\partial x_j}+\frac{\partial u_j^h}{\partial x_i}\right)\right\}d\Omega$$
$$+\sum_{e=1}^{N_e}\frac{1}{Re}\int_{\Omega^e}U^h\left[\frac{\partial\nu_{t,n}^h}{\partial x_i}\left(\frac{\partial u_i^h}{\partial x_j}+\frac{\partial u_j^h}{\partial x_i}\right)+(1+\nu_{t,n}^h)\left\{\frac{\partial}{\partial x_i}\left(\frac{\partial u_i^h}{\partial x_j}+\frac{\partial u_j^h}{\partial x_i}\right)\right\}\right]d\Omega \tag{33}$$

We assume that the following conditions hold good in our formulation:

(i) The element domains are hexahedral and u_j are interpolated with a trilinear isoparametric interpolation function
(ii) Also, we know that $\partial u_i^h/\partial x_i = 0$

The above two conditions imply that on the interior of each element

$$\frac{\partial}{\partial x_j}\left(\frac{\partial u_i^h}{\partial x_i}\right) + \frac{\partial^2 u_j^h}{\partial x_i\,\partial x_i} = 0$$

Hence, Equations (23) and (33) together will yield

$$\begin{aligned}
&\sum_{e=1}^{N_e} \int_{\Omega^e} \{\bar{W}\}\{N\}^T \left\{\frac{\mathrm{d}u_j^*}{\mathrm{d}\tau}\right\} \mathrm{d}\Omega \\
&= -\sum_{e=1}^{N_e} \int_{\Omega^e} \{\bar{W}\}\left(\{N\}^T\{u_i(\tau)\}\left\{\frac{\partial N}{\partial x_i}\right\}^T \{u_j(\tau)\}\right) \mathrm{d}\Omega - \sum_{e=1}^{N_e} \int_{\Omega^e} K\{\bar{W}\}\{N\}^T\{u_j(\tau)\}\,\mathrm{d}\Omega \\
&\quad + \sum_l \int_{\Gamma_h^l} \{W\}\left(\frac{1+v_{\mathrm{t},n}^h}{Re}\right)\left(\left\{\frac{\partial N}{\partial x_j}\right\}^T \{u_j(\tau)\}n_i + h_j\right) \mathrm{d}\Gamma \\
&\quad - \sum_{e=1}^{N_e} \frac{1}{Re} \int_{\Omega^e} \left\{\frac{\partial W}{\partial x_i}\right\}(1+v_{\mathrm{t},n}^h)\left(\left\{\frac{\partial N}{\partial x_j}\right\}^T \{u_i(\tau)\} + \left\{\frac{\partial N}{\partial x_i}\right\}^T \{u_j(\tau)\}\right) \mathrm{d}\Omega \\
&\quad + \sum_{e=1}^{N_e} \frac{1}{Re} \int_{\Omega^e} \{U\}\frac{\partial v_{\mathrm{t},n}^h}{\partial x_i}\left(\left\{\frac{\partial N}{\partial x_j}\right\}^T \{u_i(\tau)\} + \left\{\frac{\partial N}{\partial x_i}\right\}^T \{u_j(\tau)\}\right) \mathrm{d}\Omega
\end{aligned} \tag{34}$$

In the above equation, $\Gamma_h^l \in \Gamma_h$, l is the element number. Also $\cup_l \Gamma_h^l = \Gamma_h$. An explicit Euler scheme is used to expand the left-hand side of Equation (34). A second-order Adams–Bashforth scheme has been used for the convective terms. Also, the element stiffness matrix on the left-hand side of the above equation is mass lumped. With all these concepts, Equation (34) may be rewritten as

$$\begin{aligned}
&\sum_{e=1}^{N_e} \int_{\Omega^e} [\bar{W}]\,\mathrm{d}\Omega \left\{\frac{u_j^* - u_j^n}{\Delta\tau}\right\} \\
&= -\sum_{e=1}^{N_e} \int_{\Omega^e} \{\bar{W}\}\left[\frac{3}{2}\{N\}^T\{u_i^n\}\left\{\frac{\partial N}{\partial x_i}\right\}^T \{u_j^n\} - \frac{1}{2}\{N\}^T\{u_i^{n-1}\}\left\{\frac{\partial N}{\partial x_i}\right\}^T \{u_j^{n-1}\}\right] \mathrm{d}\Omega \\
&\quad - \sum_{e=1}^{N_e} K \int_{\Omega^e} \{\bar{W}\}\{N\}^T\{u_j^n\}\,\mathrm{d}\Omega + \frac{1}{Re}\sum_l \int_{\Gamma_h^l} \{W\}(1+v_{\mathrm{t},n}^h)\left(\left\{\frac{\partial N}{\partial x_j}\right\}^T \{u_i^n\}n_i + h_i\right) \mathrm{d}\Gamma \\
&\quad - \sum_{e=1}^{N_e} \frac{1}{Re} \int_{\Omega_e} \left\{\frac{\partial W}{\partial x_i}\right\}(1+v_{\mathrm{t},n}^h)\left(\left\{\frac{\partial N}{\partial x_j}\right\}^T \{u_i^n\} + \left\{\frac{\partial N}{\partial x_i}\right\}^T \{u_j^n\}\right) \mathrm{d}\Omega \\
&\quad + \sum_{e=1}^{N_e} \frac{1}{Re} \int_{\Omega_e} \{U\}\frac{\partial v_{\mathrm{t},n}^h}{\partial x_i}\left(\left\{\frac{\partial N}{\partial x_j}\right\}^T \{u_i^n\} + \left\{\frac{\partial N}{\partial x_i}\right\}^T \{u_j^n\}\right) \mathrm{d}\Omega
\end{aligned} \tag{35}$$

After some rearrangements, the above equation may be expressed as

$$\sum_{e=1}^{N_e} \text{coeff}_k \left(\frac{u_j^* - u_j^n}{\Delta\tau} \right)_q = -\sum_{e=1}^{N_e} (\text{convu}_j)_k - \sum_{e=1}^{N_e} (\text{porousu}_j)_k + \sum_l (\text{sx}_j)_k - \sum_{e=1}^{N_e} (\text{diffu}_j)_k + \sum_{e=1}^{N_e} (\text{diffpgu}_j)_k \tag{36}$$

where

$$\text{coeff}_k = \int_{\Omega^e} \bar{W}_k \, \mathrm{d}\Omega$$

$$(\text{convu}_j)_k = \int_{\Omega^e} \bar{W}_k \left[\frac{3}{2} \left(\sum_{m=1}^{N_p} N_m (u_i^n)_m \right) \left(\sum_{m=1}^{N_p} \frac{\partial N_m}{\partial x_i} (u_j^n)_m \right) - \frac{1}{2} \left(\sum_{m=1}^{N_p} N_m (u_i^{n-1})_m \right) \left(\sum_{m=1}^{N_p} \frac{\partial N_m}{\partial x_i} (u_j^{n-1})_m \right) \right] \mathrm{d}\Omega$$

$$(\text{porousu}_j)_k = K \int_{\Omega^e} \bar{W}_k \sum_{m=1}^{N_p} N_m (u_j^h)_m \, \mathrm{d}\Omega$$

$$(\text{diffu}_j)_k = \frac{1}{Re} \int_{\Omega^e} \frac{\partial W_k}{\partial x_i} (1 + v_{\text{t},n}^h)_k \left(\sum_{m=1}^{N_p} \frac{\partial N_m}{\partial x_j} (u_i^n)_m + \sum_{m=1}^{N_p} \frac{\partial N_m}{\partial x_i} (u_j^n)_m \right) \mathrm{d}\Omega$$

$$(\text{diffpgu}_j)_k = \frac{1}{Re} \int_{\Omega^e} U_k \left(\sum_{m=1}^{N_p} \frac{\partial N_m}{\partial x_i} (v_{\text{t},n}^h)_m \right) \left(\sum_{m=1}^{N_p} \frac{\partial N_m}{\partial x_j} (u_i^n)_m + \sum_{m=1}^{N_p} \frac{\partial N_m}{\partial x_i} (u_j^n)_m \right) \mathrm{d}\Omega$$

$$(\text{sx}_j)_k = \frac{1}{Re} \int_{\Gamma_h^l} W_k (1 + v_{\text{t},n}^h)_k \left(\sum_{m=1}^{N_p} \frac{\partial N_m}{\partial x_j} (u_i^n)_m n_i + h_j \right) \mathrm{d}\Gamma$$

It may be mentioned that k is the local node of an element.

Now Equation (36) can be rewritten as

$$\sum_{e=1}^{N_e} \text{coeff}_k \left(\frac{u_j^* - u_j^n}{\Delta\tau} \right)_q = -\sum_{e=1}^{N_e} \{(\text{convu}_j)_k + (\text{porousu}_j)_k + (\text{diffu}_j)_k - (\text{diffpgu}_j)_k\} + \sum_l (\text{sx}_j)_k \tag{37}$$

or

$$\left(\frac{u_j^* - u_j^n}{\Delta\tau} \right)_q \sum_{n_q} \text{coeff}_k = -\sum_{n_q} (\text{tderu}_i)_k \tag{38}$$

where n_q are the elements which have q as common node point. Then, at each global node q, the contribution from the neighboring elements will yield

$$\text{gcoeff}_q = \sum_{n_q} \text{coeff}_k, \qquad (\text{gtderu}_j)_q = -\sum_{n_q} (\text{tderu}_j)_k \tag{39}$$

As mentioned earlier, k are the local nodes of element n_q and these correspond to the global node q. Finally, at each node q, we get

$$\left(\frac{u_j^* - u_j^n}{\Delta\tau}\right)_q = \frac{(\text{gtderu}_j)_q}{\text{gcoeff}_q}, \qquad (u_j^*)_q = (u_j^n)_q + \Delta\tau \frac{(\text{gtderu}_j)_q}{\text{gcoeff}_q} \tag{40}$$

2.6. Choice of SUPG test (weighting) functions

The perturbation term of weighting function $\bar{W}^h$ is defined by

$$U^h = \frac{\tilde{k}}{\|\mathbf{u}\|^2} u_i \frac{\partial W^h}{\partial x_i} \tag{41}$$

Hence

$$\bar{W}^h = W^h + \frac{\tilde{k}}{\|\mathbf{u}\|^2} u_i \frac{\partial W^h}{\partial x_i}$$

where W^h is same as trial functions

$$W^h = \{W\} = \{N\}$$

Therefore,

$$\{\bar{W}\} = \{N\} + \frac{\tilde{k}}{\|\mathbf{u}\|^2} \left\{u_i \frac{\partial N}{\partial x_i}\right\} \tag{42}$$

The weighting function for local node k can be expressed as

$$\bar{W}_k = N_k + \frac{\tilde{k}}{\|\mathbf{u}\|^2} \left\{u_i \frac{\partial N_k}{\partial x_i}\right\} \tag{43}$$

where $\|\mathbf{u}\|^2 = u_i u_i$.

Assuming the advective movement on the element scale is locally one-dimensional, the parameters $\tilde{k}$, $\|\mathbf{u}\|$, and u_i are to be evaluated at the element center ($\xi = \eta = \zeta = 0$) as follows:

$$\tilde{k} = \frac{\alpha \|\mathbf{u}\| h}{\sqrt{15}} \tag{44}$$

where

$$\alpha = \coth(Pe) - \frac{1}{Pe}$$

where Pe is the cell Peclet number

$$Pe = \frac{\|\mathbf{u}\|h}{2\tilde{k}}$$

$$h = 2(|h_1| + |h_2| + |h_3|) \tag{45}$$

where h_1, h_2, and h_3 are the projections of $\vec{e}_\xi$, $\vec{e}_\eta$, and $\vec{e}_\zeta$ vectors in the direction of the local flow velocity $\mathbf{u}$. The vectors $\vec{e}_\xi$, $\vec{e}_\eta$, and $\vec{e}_\zeta$ are in the ξ-, η-, and ζ-directions respectively. The projections h_1, h_2, h_3 may be expressed as

$$h_1 = \frac{1}{\|\mathbf{u}\|}(u_i(x_i)_\xi), \qquad h_2 = \frac{1}{\|\mathbf{u}\|}(u_i(x_i)_\eta), \qquad h_3 = \frac{1}{\|\mathbf{u}\|}(u_i(x_i)_\zeta) \tag{46}$$

Finally the Cartesian derivatives are evaluated in terms of the normalized ξ, η, and ζ co-ordinates. The elemental integrals are expressed in terms of the determinant of the Jacobian matrix, $d\xi$, $d\eta$, and $d\zeta$. Two-point Gauss–Legendre quadrature is used to perform the numerical integration.

3. RESULTS AND DISCUSSION

3.1. The flow field in a plate-spiral

The present simulation has been performed for a Reynolds number of 10^6 using the same value of Darcy's coefficient, K, as reported by Shyy and Vu [10]. The variation of K along the distributor height and in the circumferential direction has been considered in the present computation. Table I represents the Darcy's coefficient used in the computation. Figure 3 has to be consulted to identify the elements in Table I.

Figure 4 shows the predicted velocity vectors on the horizontal mid-plane of the casing. It can be seen that the uniform velocity at the entrance gradually culminates into a forced vortex within the casing. This is in contrast with the free vortex flow as observed in the case of conventional spiral casing (see Maji and Biswas [16]).

Figure 5 shows the static pressure variation on the same horizontal mid-plane of the casing. The static pressure varies primarily along the radial direction. However, near the stay vane inlet and in the distributor region, the static pressure is almost equal to the local ambient pressure. The centrifugal force $\rho v_\theta^2/r$ is balanced by the radial pressure gradient $\partial p/\partial r$. A high-pressure gradient exists near the outer periphery of the spiral due to large value of peripheral velocity. The effect of radial pressure gradient can be clearly seen from the strong secondary velocity vectors shown in the next figure. An imbalance between the centrifugal force and radial pressure gradient causes the development of secondary flow.

Table I. Darcy's coefficient used in the computation.

Element location		Non-dimensionalized K	
θ (°)	Element between the planes	Elements located between $J = 1$ and 4, $J = 6$ and 9	Elements located between $J = 4$ and 6
358	13 and 14	0.375	0.375
5.5	14 and 15	0.506	0.506
23.5	15 and 16	0.560	0.560
41.5	16 and 17	0.480	0.480
59.5	17 and 18	0.370	0.460
77.5	18 and 19	0.340	0.460
95.5	19 and 20	0.340	0.440
113.5	20 and 21	0.340	0.420
131.5	21 and 22	0.340	0.400
149.5	22 and 23	0.340	0.380
167.5	23 and 24	0.330	0.370
185.5	24 and 25	0.320	0.360
203.5	25 and 26	0.310	0.360
221.5	26 and 27	0.300	0.350
239.5	27 and 28	0.300	0.350
257.5	28 and 29	0.300	0.380
275.5	29 and 30	0.300	0.440
293.5	30 and 31	0.300	0.510
311.5	31 and 32	0.300	0.991
329.5	32 and 33	0.300	1.194
347.5	33 and 34	0.300	0.755

J is the grid index along axial direction.

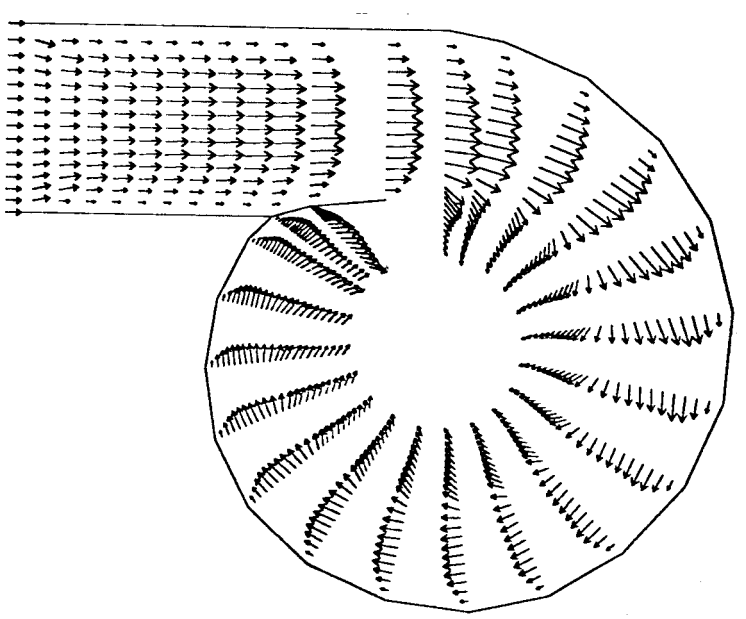

Figure 4. Velocity vectors on a horizontal mid-plane for $Re = 10^6$.

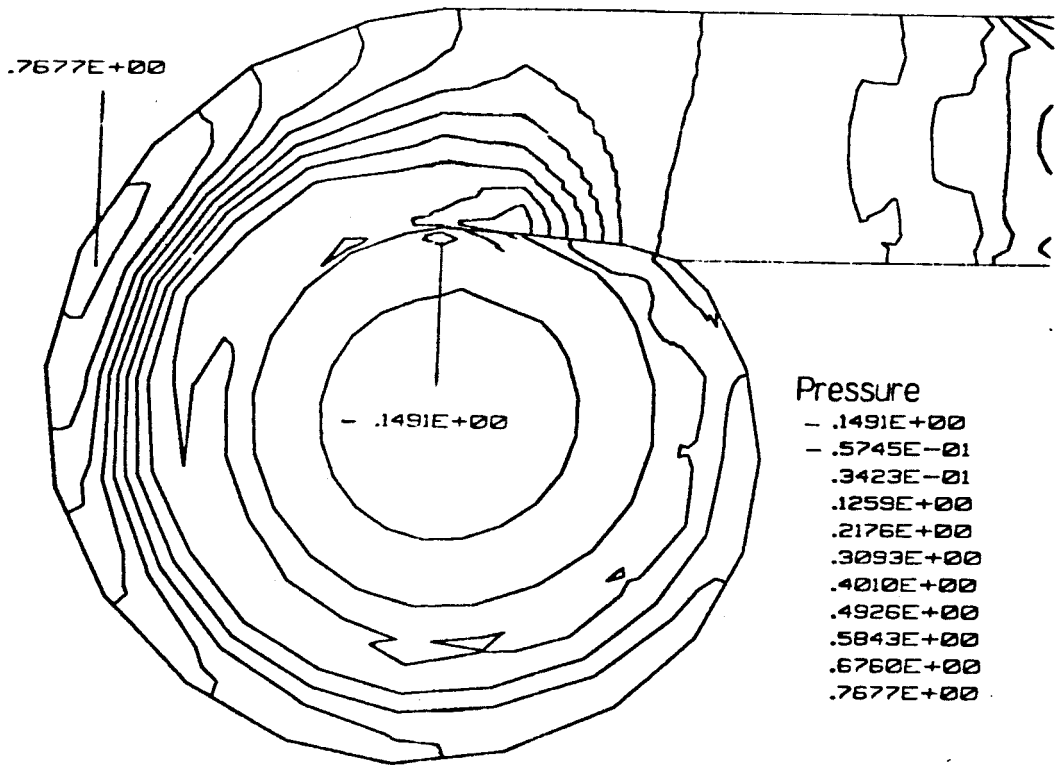

Figure 5. Static pressure distribution over the horizontal mid-plane for $Re = 10^6$.

Figure 6 depicts the behavior of the secondary flow at six different cross-stream planes located at $\theta = 11°$, 65°, 83°, 155°, 191°, and 263°. Several factors influence the development of the secondary flow. The secondary flow exhibits strong inward motion close to the top and the bottom wall region together with double counter rotating vortices near the core region. The strong inward flow near the wall induces boundary layer suction effects similar to that in the conventional spiral. The strength of the secondary flow varies in the circumferential direction. At the beginning ($\theta = 11°$) of the plate spiral (Figure 6(a)), the double vortices are very weak. However, at $\theta = 65°$ and 83° (see Figure 6(b) and (c)), these vortices are more prominent. After a 155° turn (Figure 6(d)) the secondary flow continues to persist. However, in this case, the double vortices are somewhat weaker. After a 263° turn (Figure 6(f)), the double vortices disappear due to the acceleration of flow in the radial direction. In all the sections, flow is parallel in the distributor region.

Figure 7 shows the static pressure contours at four different cross-sections located at $\theta = 11°$, 83°, 191°, and 263°. The static pressure decreases from the outside wall of the casing towards the distributor outlet. It can be seen from these figures that a low-pressure zone is

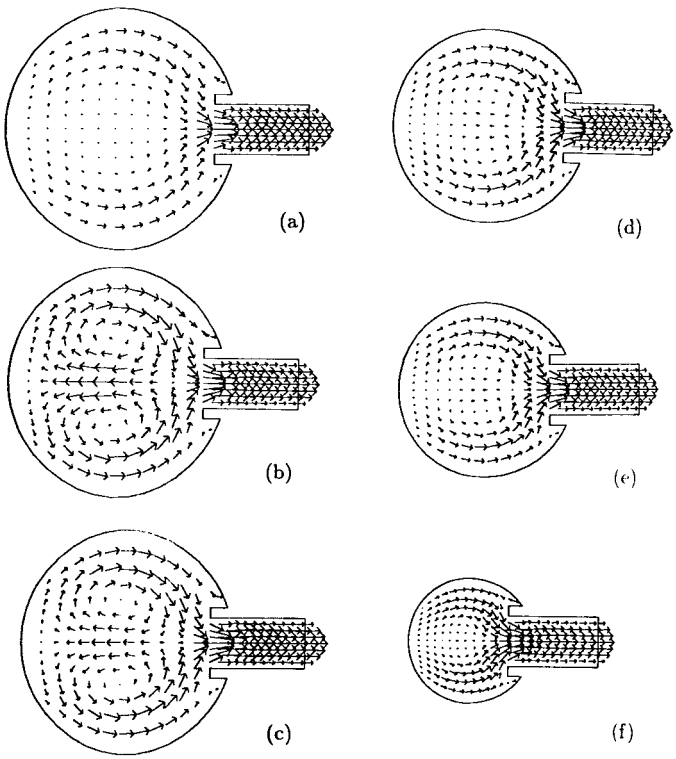

Figure 6. Secondary flow at different cross-sections for $Re = 10^6$: (a) $\theta = 11°$, (b) $\theta = 65°$, (c) $\theta = 83°$, (d) $\theta = 155°$, (e) $\theta = 191°$, (f) $\theta = 263°$.

created near the stay vane inlet. This induces circulatory motion. It can also be seen that throughout the distributor, the static pressure is constant and equal to the static pressure at the exit of the distributor.

The total pressure contours on the same cross-stream planes are shown in Figure 8. Total pressure is maximal at the center while it is minimal near the wall. This distribution agrees well with the observation of Kurokawa and Nagahara [17] in a conventional spiral casing.

3.2. Prediction of pertinent performance parameters

Figure 9 explains some of the important zones on a cross-stream plane. Distribution of various flow parameters in these zones characterizes the performance of a spiral casing.

The radial distribution of flow parameters for four different cross-sectional planes located at $\theta = 11°$, 83°, 191°, and 263° along HH (Figure 9) is shown in Figure 10. The static pressure, p, decreases towards the inner radius and becomes equal to the ambient pressure near the stay vane inlet (r/r_{sv}). Within the distributor, also, the static pressure remains constant. The total

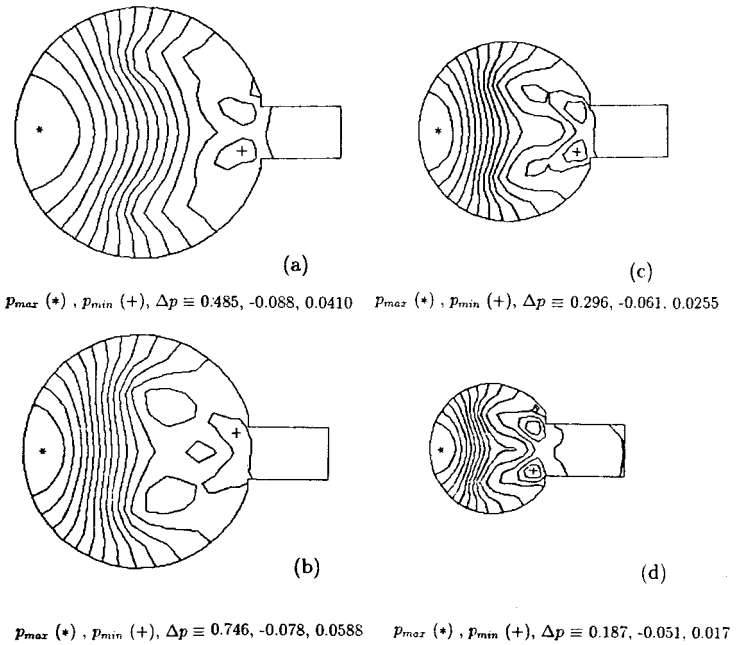

Figure 7. Static pressure contour at different cross-sections for $Re = 10^6$: (a) $\theta = 11°$, (b) $\theta = 83°$, (c) $\theta = 191°$, (d) $\theta = 263°$.

pressure, p_t, at first increases from the outside wall to the inner radius and then keeps decreasing up to the distributor exit. The radial velocity, v_r, is directed towards the outer wall except near the stay vane ($r/r_{sv} = 1$) zone. Here, it changes direction and increases rapidly. However, within the distributor zone it remains almost constant. It can be seen that a weak inward radial velocity is induced for $\theta \geq 191°$ near the outer radius. The axial velocity, v, is zero along HH on all the cross-stream planes. The tangential velocity, v_θ, increases from the outside wall towards the center core region and then keeps decreasing up to the distributor exit. Within the distributor, the tangential velocity keeps on increasing along the circumferential direction, while the radial velocity decreases slowly.

The axial distribution of the flow parameters along VV (refer to Figure 9) is shown in Figure 11. The parametric study has been carried out for four different cross-sectional planes located at $\theta = 11°$, 63°, 191°, and 263°. A low total pressure zone near the wall and a high total pressure zone at the center are seen in all the sections. The distribution pattern of tangential velocity is commensurate with the distribution pattern of total pressure. Both total pressure and tangential velocity decrease in the circumferential direction. The radial velocity distribution at $\theta = 11°$ (Figure 11(a)) also reveals the existence of very weak outward flow at the center and relatively stronger inward flow near the wall. Both the inward and outward radial flows are much stronger at $\theta = 83°$ (Figure 11(b)). However, at $\theta \geq 191°$ (Figure 11(c) and (d)), the outward flow is quite weak whereas the inward flow becomes much stronger.

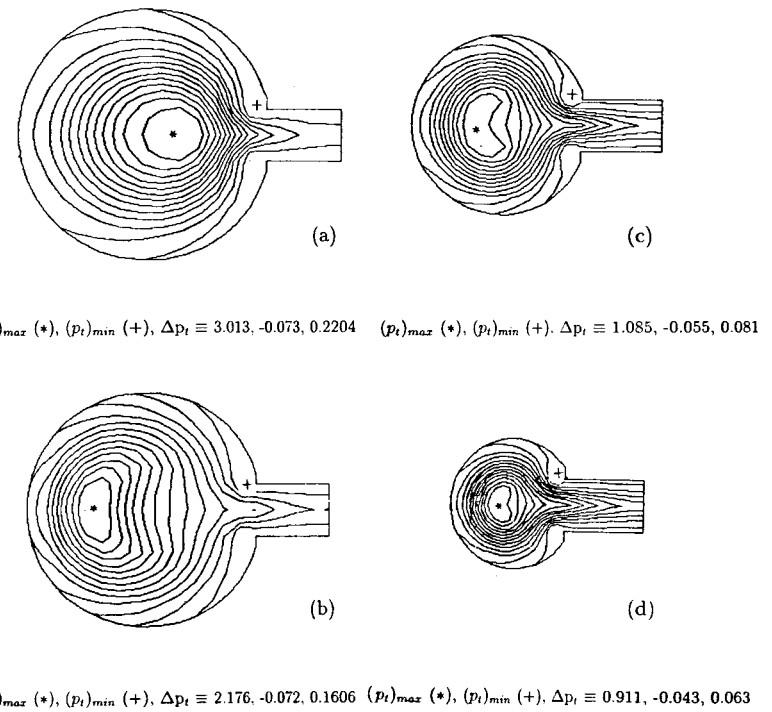

Figure 8. Total pressure contour at different cross-sections for $Re = 10^6$: (a) $\theta = 11°$, (b) $\theta = 83°$, (c) $\theta = 191°$, (d) $\theta = 263°$.

The axial distribution of flow parameters along SS (refer to Figure 9) is shown in Figure 12. The study has been focused on for four different cross-sectional planes located at $\theta = 11°$, 83°, 191°, and 263°. A low total pressure zone near the wall and a high total pressure zone around the mid-height is seen in all the sections. The static pressure and axial velocity along SS are almost zero. The peripheral velocity, v_θ, decreases in the range $11° \leq \theta \leq 83°$. However, the same is accelerated after $\theta > 83°$. The radial component of velocity increases in the range $11° \leq \theta \leq 83°$. However, the same is decelerated after $\theta > 83°$. The total pressure does not change in the circumferential direction.

The axial distribution of flow characteristics at the exit of the guide vane channel (along GG in Figure 9) for four different angles ($\theta = 11°$, 83°, 191°, and 263°) is shown in Figure 13. The radial velocity reduces while the tangential velocity increases in the circumferential direction. At the exit of the guide vanes, the static pressure is equal to the local ambient pressure. The total pressure does not change in the circumferential direction. The axial velocity is almost zero in all the sections, which signifies that the flow is nearly two-dimensional in the distributor region.

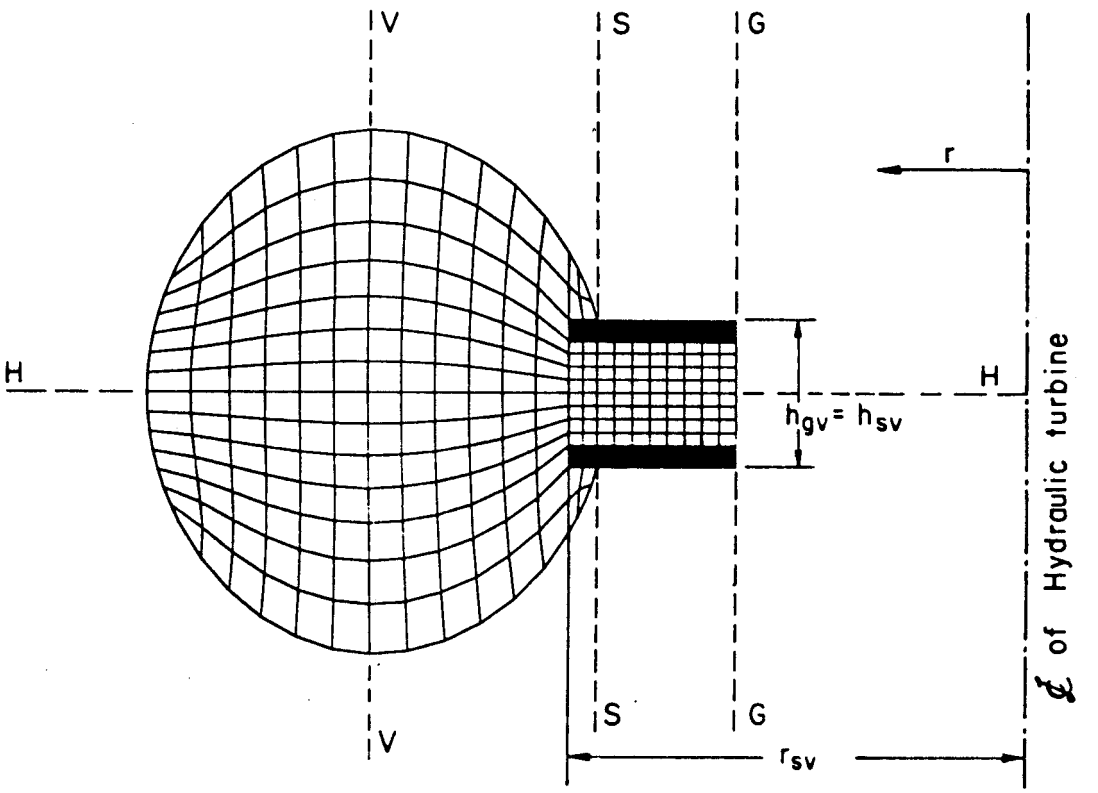

Figure 9. Important zones on the cross-stream plane.

Figure 14 depicts distribution of the mean flow parameters over VV along the circumferential direction. Average total pressure, $\overline{p_t}$, decreases in the main flow direction. Average static pressure, $\bar{p}$, remains constant along the circumferential direction. Average tangential velocity, $\overline{v_\theta}$, decreases in the circumferential direction. Average radial velocity, $\overline{v_r}$ increases in the same direction except for the zone near the inlet of the spiral.

In order to examine the variation of mean flow parameters along the circumferential direction, the averaged values of pressure and velocity over the GG section are plotted as a function of angular position in Figure 15. The tangential velocity increases slightly in the circumferential direction. As a result, the total pressure also increases in the same direction. The static pressure is equal to the local ambient pressure and axial velocity is found to be zero.

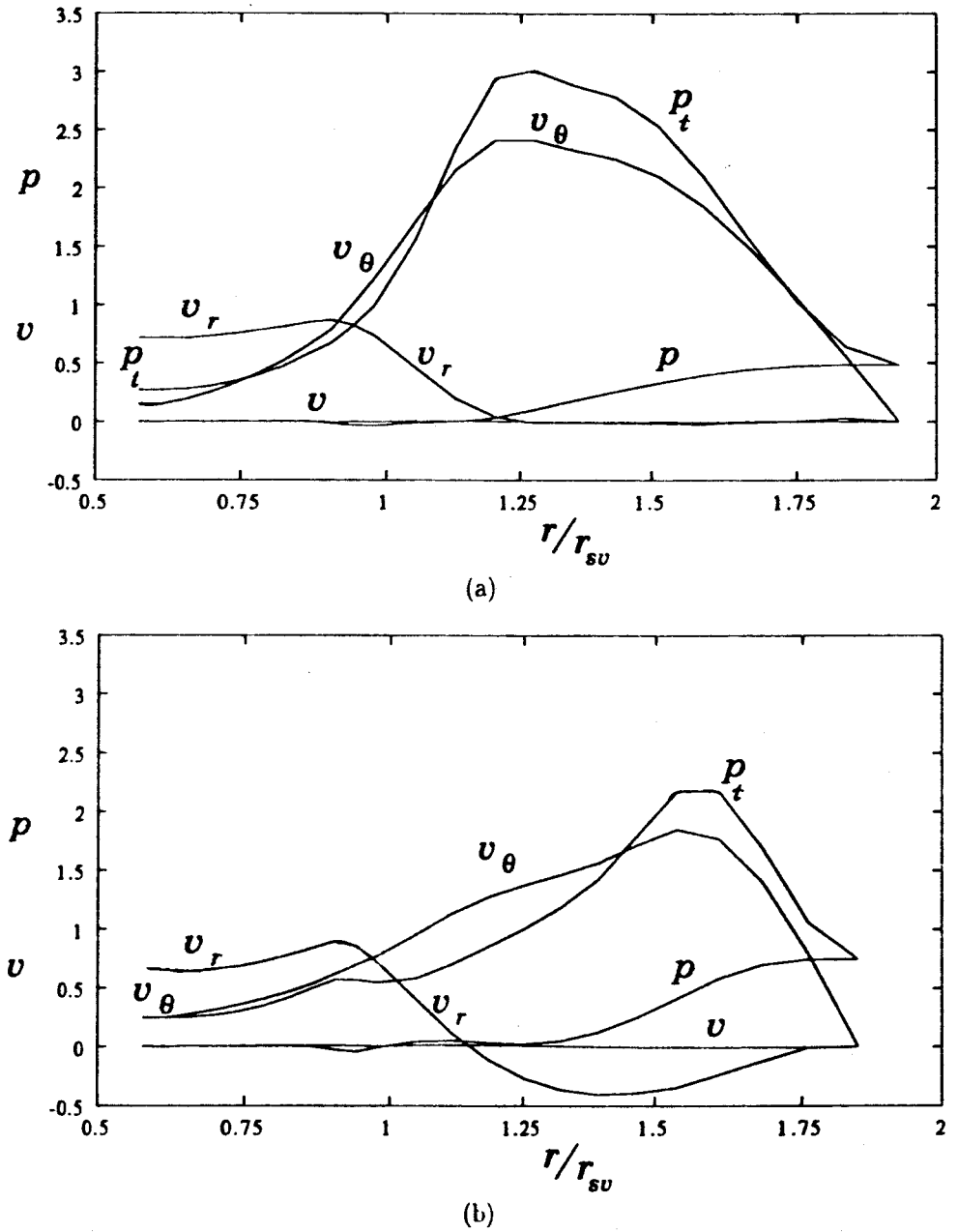

Figure 10. Radial distribution of flow parameters along HH at (a) $\theta = 11°$, (b) $\theta = 83°$, (c) $\theta = 263°$, (d) $\theta = 191°$ for $Re = 10^6$.

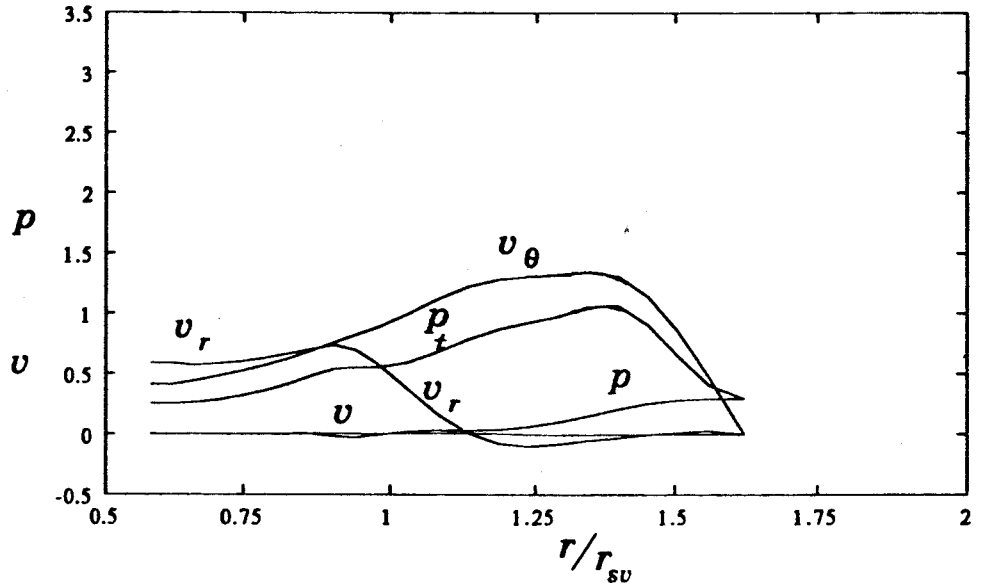

(c)

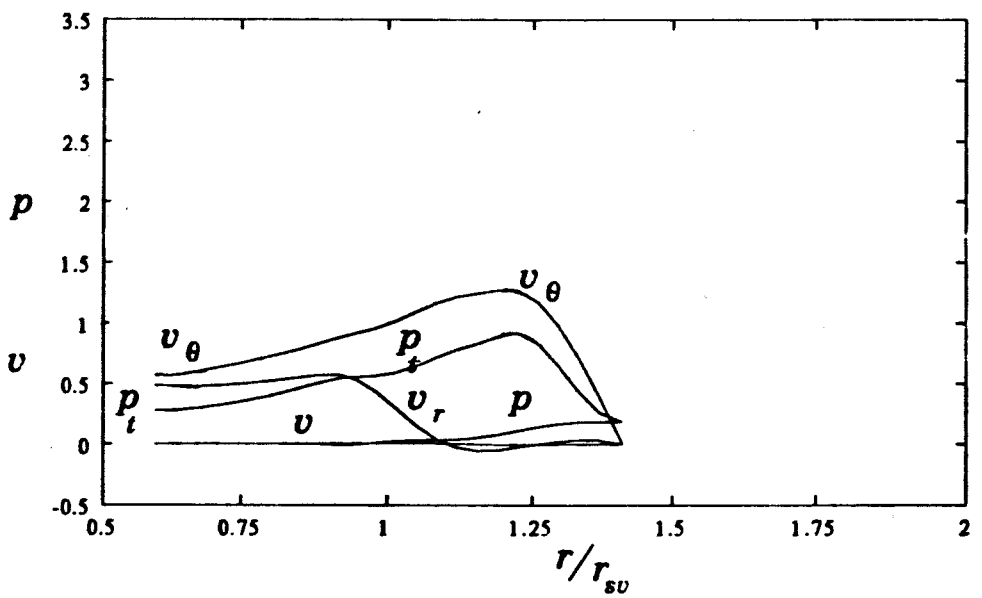

(d)

Figure 10 (*Continued*)

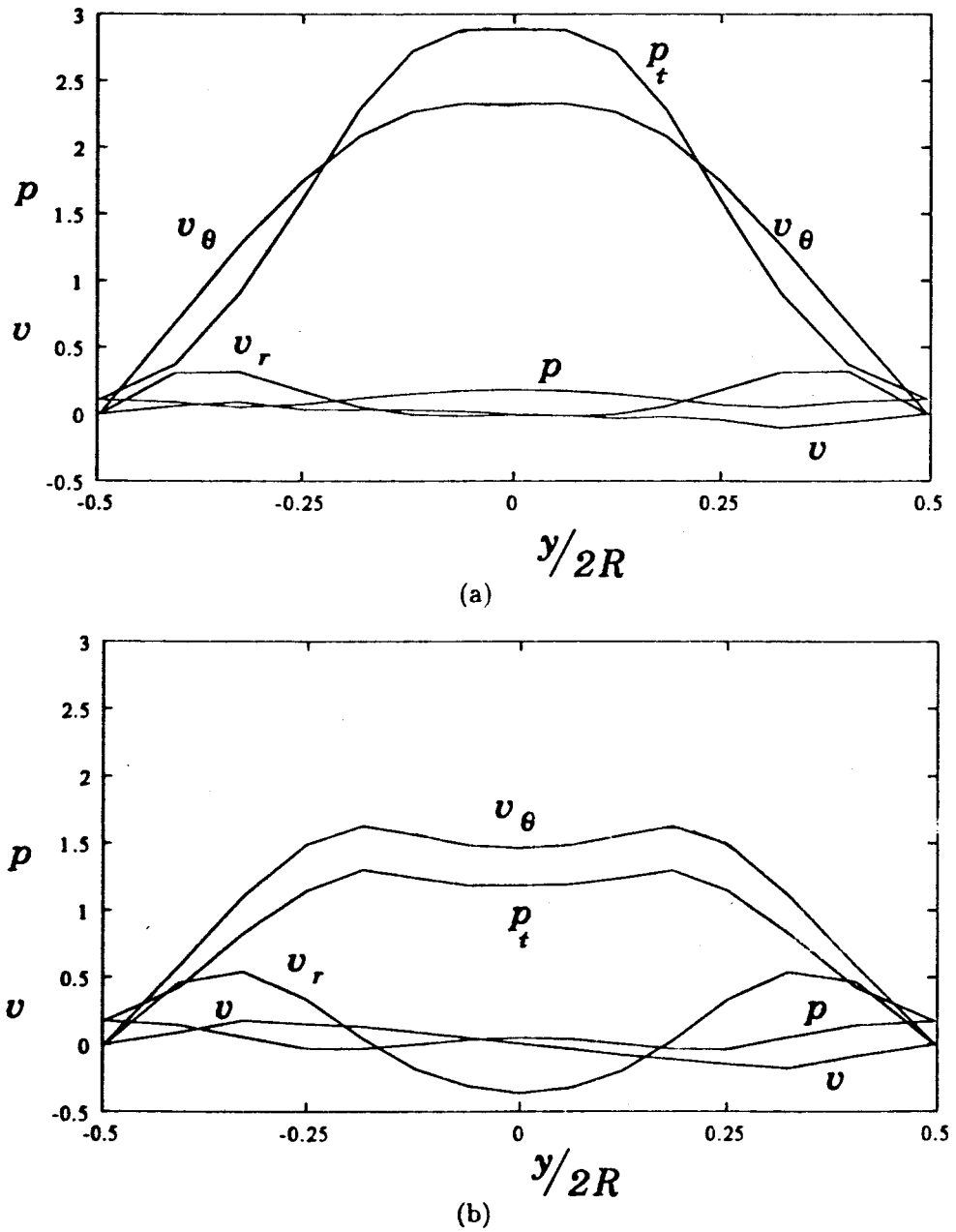

Figure 11. Axial distribution of flow parameters along VV at (a) $\theta = 11°$, (b) $\theta = 83°$, (c) $\theta = 263°$, (d) $\theta = 191°$ for $Re = 10^6$.

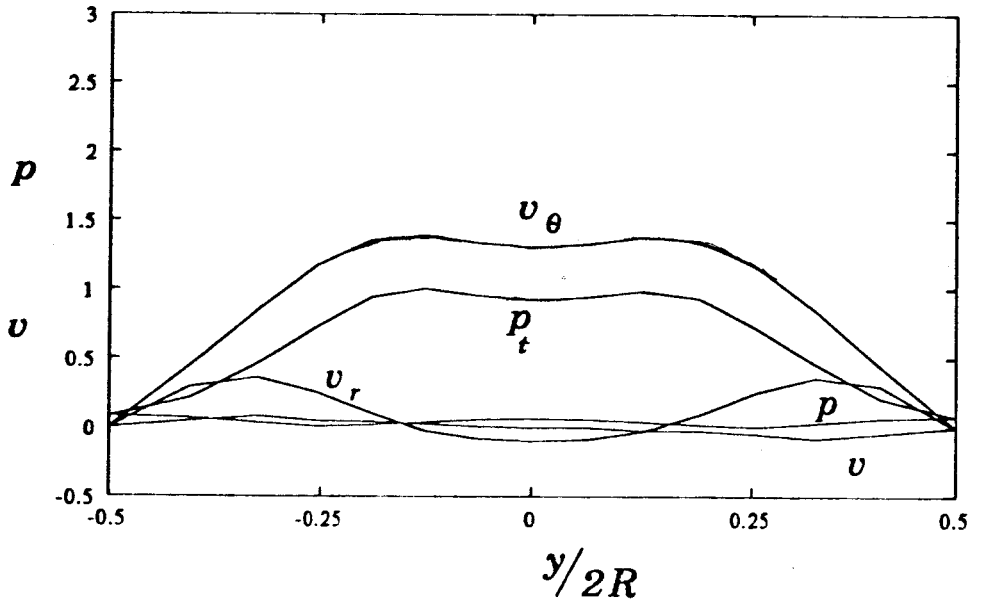

(c)

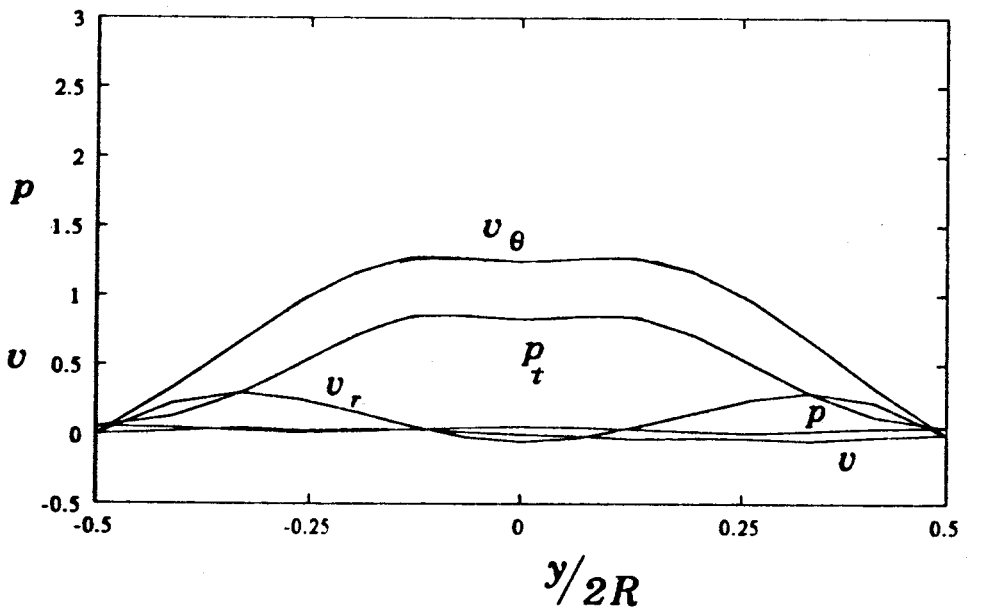

(d)

Figure 11 (*Continued*)

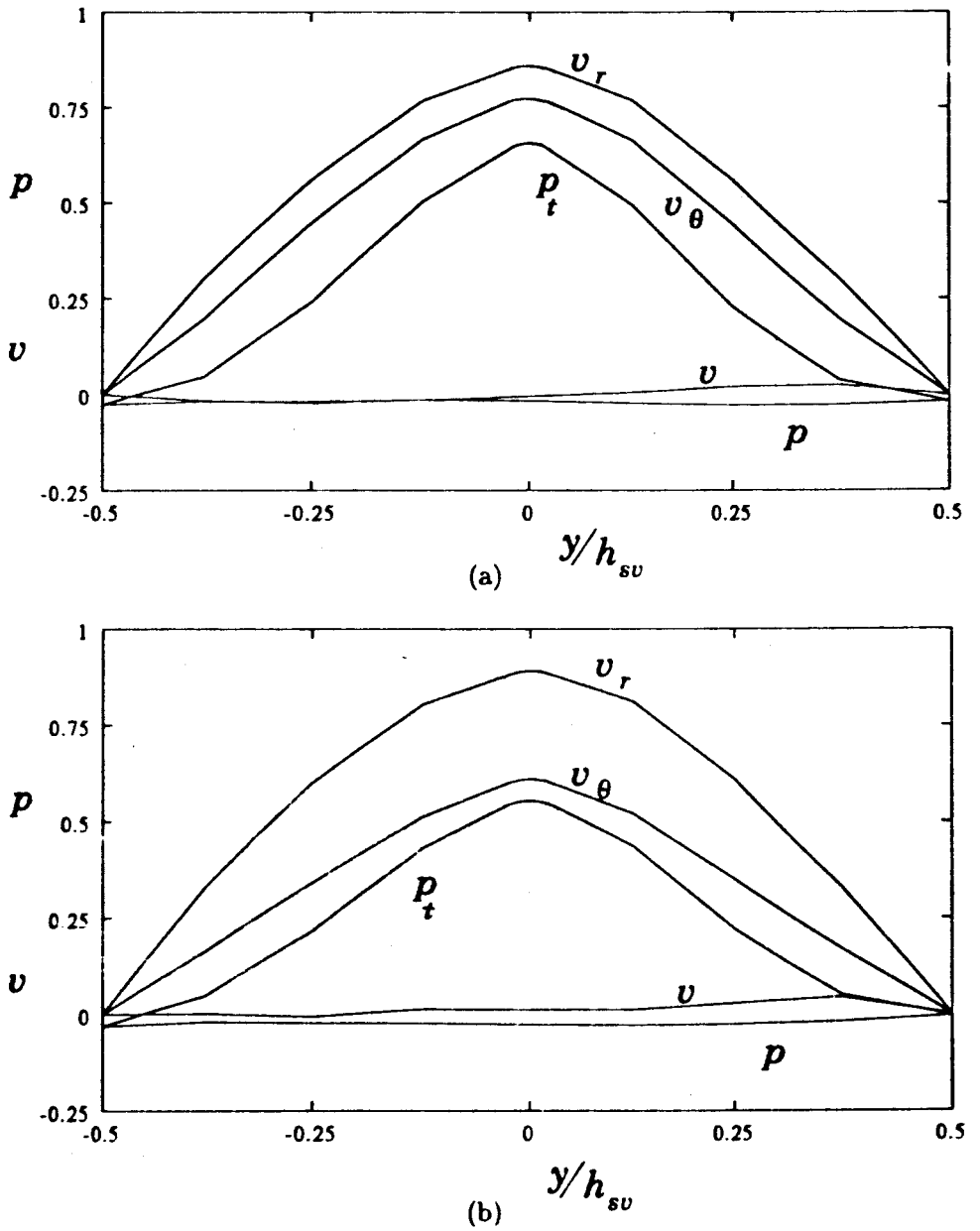

Figure 12. Axial distribution of flow parameters along SS at (a) $\theta = 11°$, (b) $\theta = 83°$, (c) $\theta = 191°$, (d) $\theta = 263°$ for $Re = 10^6$.

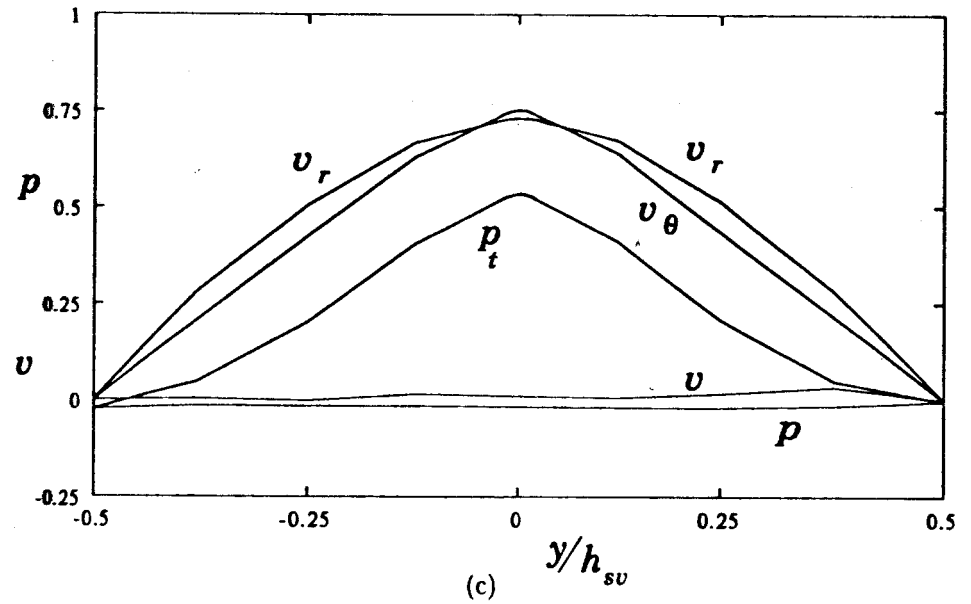

(c)

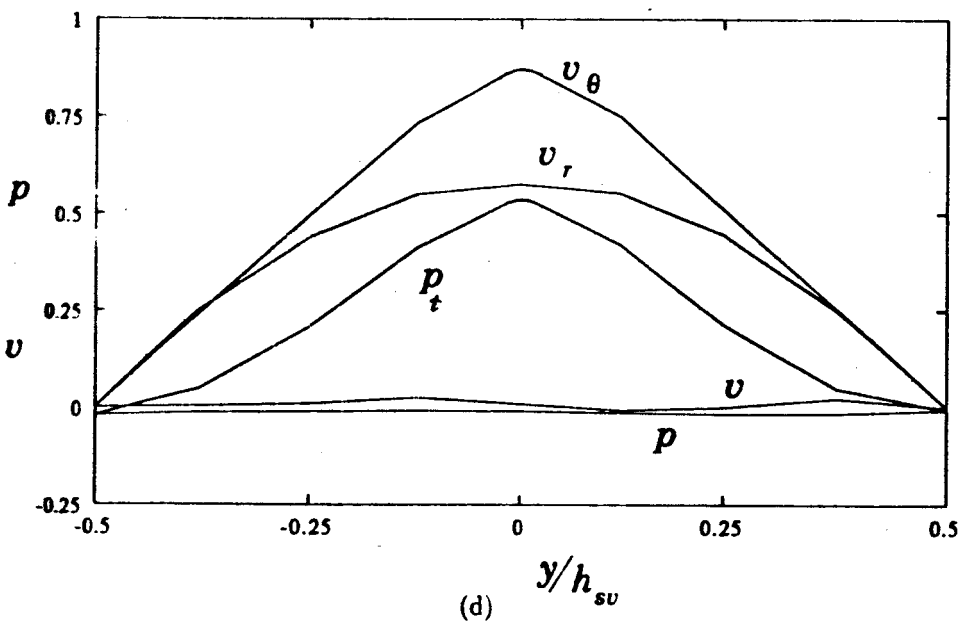

(d)

Figure 12 (*Continued*)

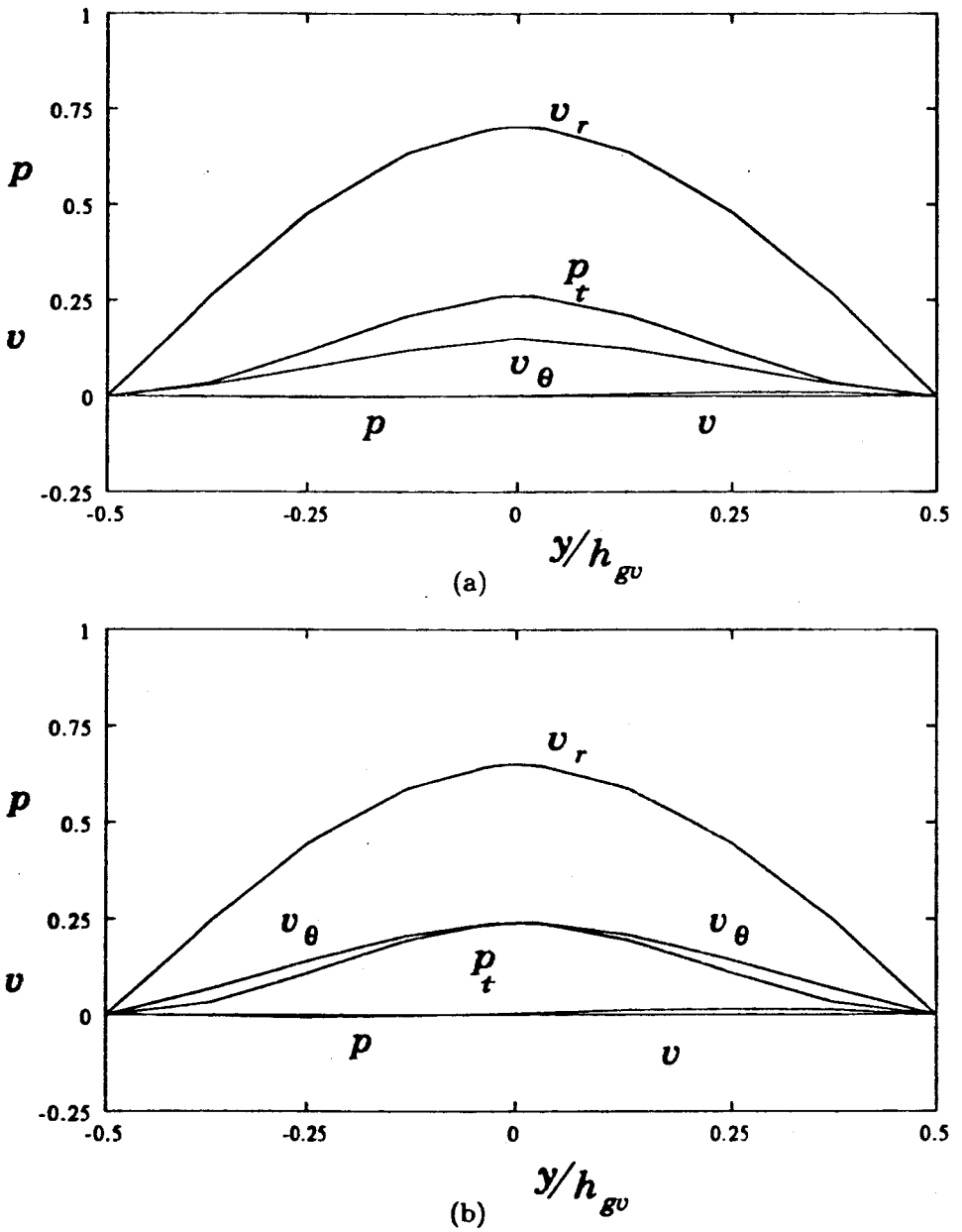

Figure 13. Axial distribution of flow parameters along GG at (a) $\theta = 11°$, (b) $\theta = 83°$, (c) $\theta = 191°$, (d) $\theta = 263°$ for $Re = 10^6$.

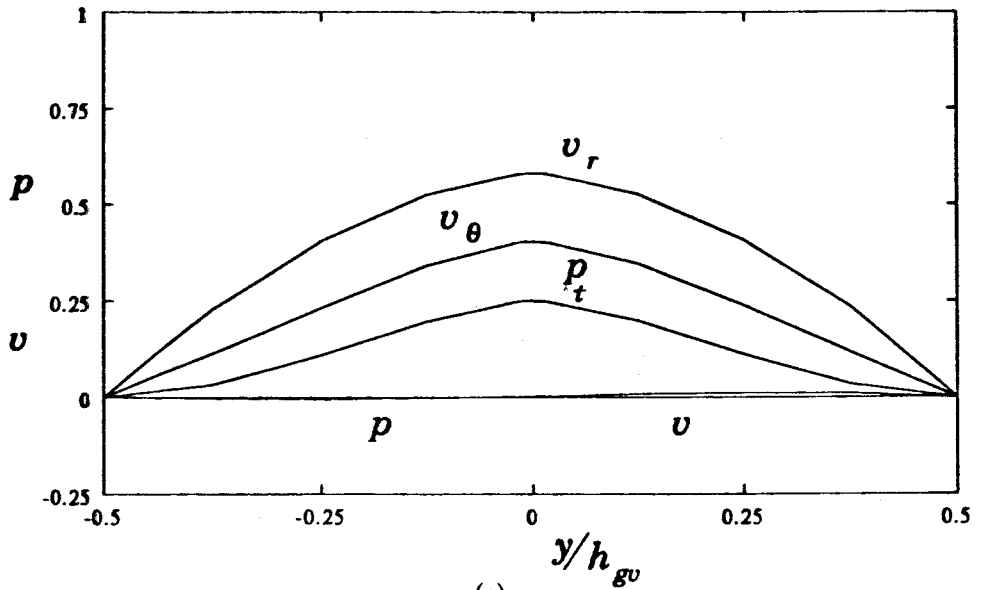

(c)

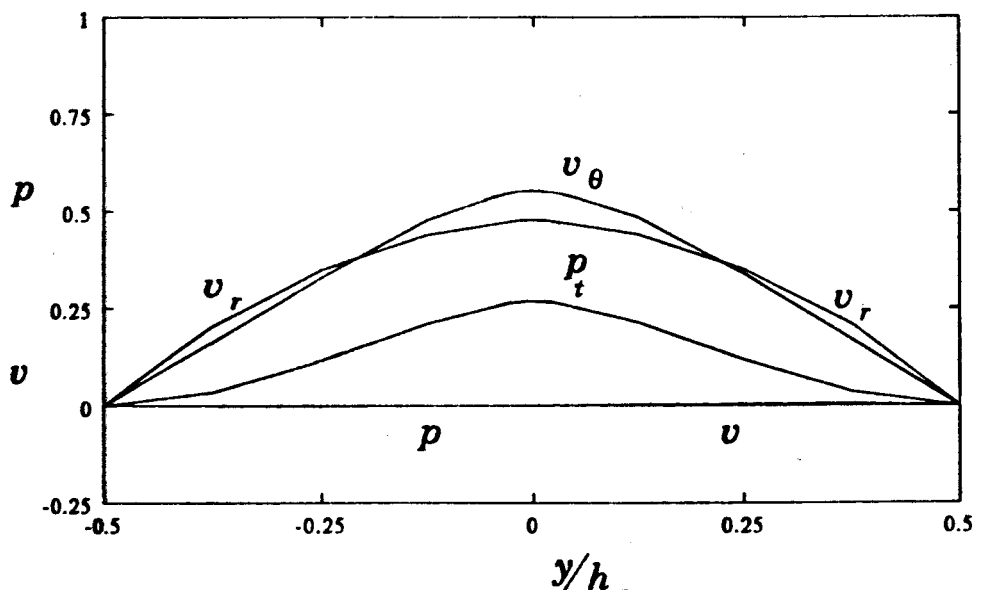

(d)

Figure 13 (*Continued*)

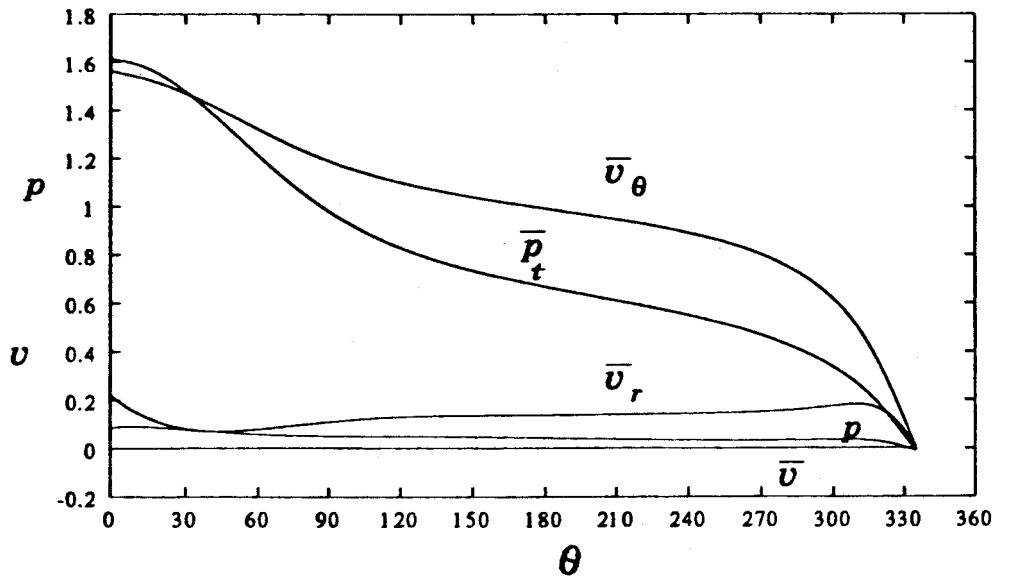

Figure 14. Average flow characteristics on the VV-section as a function of θ.

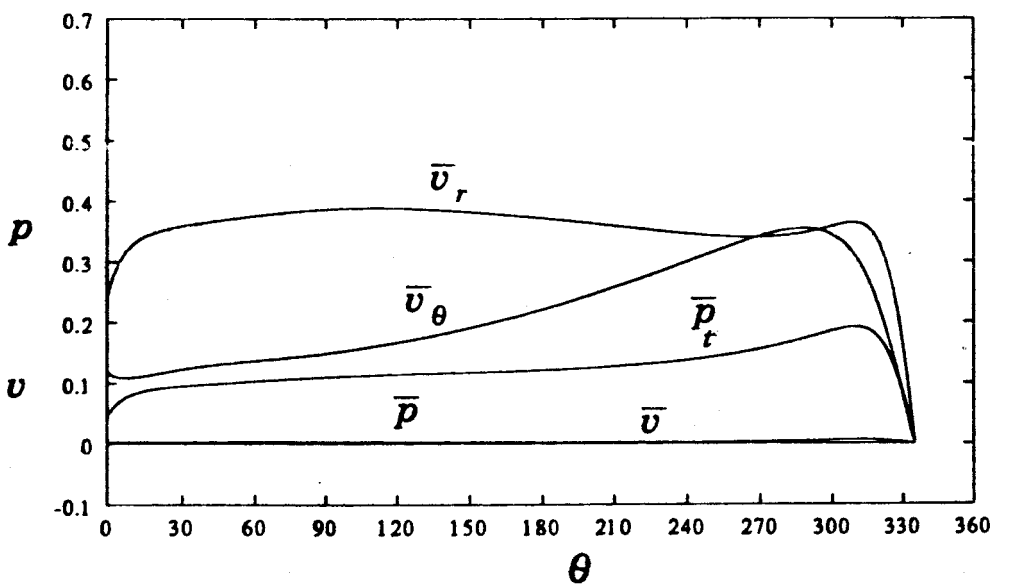

Figure 15. Average flow characteristics on the GG-section as a function of θ.

4. CONCLUSIONS

The optimum performance of a spiral casing is an increasingly important concern of turbine manufacturers. The plate-spirals are being considered by the turbine manufacturers for the simplicity of the manufacturing process. However, the performance of the plate-spirals is not known. The performances of such spiral casings have to be evaluated and the pertinent parameters should be optimized. The need for a computational fluid dynamics tool for such optimization has been felt over the past decade. The present investigation explains the utility of such a computational tool. Three-dimensional flow and pressure distribution in a novel spiral casing have been obtained using a SUPG technique. The results thus obtained show a plausible physical situation. The development of a useful model for such a complex geometry may be attributed to mathematical accuracy of the SUPG technique. Earlier, the method was successfully deployed by the authors [16] for analyzing flow through a conventional spiral casing. The present investigation is an extension of the earlier study. As such, the contribution of this investigation is in the effective utilization of an elegant mathematical concept. The results reveal a plausible three-dimensional turbulent flow in an extremely complex geometrical configuration of practical interest. The task that has to be taken up in future is the accomplishment of the model validation through comparison with the experimental results.

REFERENCES

1. Sopta L, Mrsa Z. Numerical modeling of three-dimensional flow in the spiral casing of a Francis turbine. In *International Conference on Hydraulic Machinery*, Ljubljana, 1988; 85–90.
2. Mrsa Z. Optimal design of spiral casing tongue and wicket gate angle by decomposition method. *International Journal for Numerical Methods in Fluids* 1993; **17**: 995–1002.
3. Ulrich D. Berechnung der laminaren stromung in einem turbinenspiralgehause mittels einer finiti-element-formulierung der navier-stokes-gleichungen in nicht-druckintegrierter form. *Ingenieur Archiv (Archive of Applied Mechanics)* 1986; **56**: 192–200.
4. Shyy W, Vu TC. A numerical study of incompressible Navier–Stokes flow through rectilinear and radial cascade of turbine blades. *Computers in Mechanics* 1986; **1**: 269–279.
5. Vu TC, Shyy W, Braaten ME, Reggio M. Recent development in viscous flow analysis for hydraulic turbine components. In *IAHR Symposium 1986*, 2, Montreal, Canada, 1986.
6. Vu TC, Shyy W. Navier–Stokes computation of radial inflow turbine distributor. *ASME Journal of Fluid Engineering* 1988; **110**: 29–32.
7. Vu TC, Shyy W. Viscous flow analysis as a design tool for hydraulic turbine components. *ASME Journal of Fluid Engineering* 1990; **112**: 5–11.
8. Vu TC, Shyy W. Navier–Stokes flow analysis for hydraulic turbine draft tubes. *ASME Journal of Fluid Engineering* 1990; **112**: 199–204.
9. Shyy W, Vu TC. On the adoption of velocity variable and grid system for fluid flow computation in curvilinear coordinates. *Journal of Computational Physics* 1991; **92**: 82–105.
10. Shyy W, Vu TC. Modeling and computation of flow in a passage with 360-degree turning and multiple airfoils. *ASME Journal of Fluid Engineering* 1993; **115**: 103–108.
11. Sundararajan T. Automatic grid generation for complex geometry problem. In *Computational Fluid Flow and Heat Transfer*, Muralidhar K, Sundararajan T (eds). Narosa Publishing House: India, 1995.
12. Brooks AN, Hughes TJR. Streamline upwind/Petrov–Galerkin formulation for convection dominated flows with particular emphasis on the incompressible Navier–Stokes equation. *Computational Methods in Applied Mechanics and Engineering* 1982; **32**: 199–259.
13. Chorin AJ. A numerical method for solving incompressible viscous flow problems. *Journal of Computational Physics* 1967; **2**: 12–26.

14. Harlow FH, Welch JE. Numerical calculation of time dependent viscous incompressible flow of fluid with free surface. *The Physics of Fluids* 1965; **8**: 2182–2188.
15. Donea J, Giuliani S, Laval H. Finite element solution of the unsteady Navier–Stokes equation by fractional step method. *Computational Methods in Applied Mechanics and Engineering* 1982; **30**: 53–73.
16. Maji PK, Biswas G. Analysis of flow in the spiral casing using a streamline upwind Petrov–Galerkin method. *International Journal for Numerical Methods in Engineering* 1999; **45**: 147–174.
17. Kurokawa J, Nagahara H. Flow characteristic in spiral casing of water turbine. In *IAHR Symposium 1986*, 2, Paper No. 62, Montreal, Canada, 1986.

